ADVANCED FUNCTIONAL MATERIALS
www.afm-journal.de

Phase Engineering for Stability of $CsPbI_3$ Nanowire Optoelectronics

*Dengji Li, Pengshan Xie, Yuxuan Zhang, You Meng, Yancong Chen, Yini Zheng, Weijun Wang, Di Yin, Bowen Li, Zenghui Wu, Changyong Lan, SenPo Yip, Dangyuan Lei, Fu-Rong Chen, and Johnny C. Ho**

Zinc (Zn) has arisen as a significant suppressor of vacancy formation in halide perovskites, establishing its pivotal role in defect engineering for these materials. Herein, the Zn-catalyzed vapor-liquid-solid (VLS) route is reported to render black-phase $CsPbI_3$ nanowires (NWs) operationally stable at room temperature. Based on first-principle calculations, the doped Zn^{2+} can not only lead to the partial crystal lattice distortion but also reduce the formation energy (absolute value) from the black phase to the yellow phase, improving the stability of the desired black-phase $CsPbI_3$ NWs. A series of contrast tests further confirm the stabilization effect of the Zn-doped strategy. Besides, the polarization-sensitive characteristics of black-phase $CsPbI_3$ NWs are revealed. This work highlights the importance of phase stabilization engineering for $CsPbI_3$ NWs and their potential applications in anisotropic optoelectronics.

The crystallization of halide perovskites (HPs) into 1D structures has generated considerable research interest for their promising prospects in studying electron transport characteristics and multifunctional nanoscale devices.[1] To date, various strategies have been developed to achieve in-plane growth of 1D structures, including epitaxy,[2] capillary-bridge-manipulated graphoepitaxy,[3] and van der Waals epitaxy.[4] Typically, the VLS growth mode,[5] which involves the initial seeding of metallic catalytic nanoparticles to facilitate the process, has realized the out-of-plane and bottom-up synthesis route, opening up a new pathway for the 1D perovskite electronics and optoelectronics.

Iodine-based inorganic halide perovskites (IHPs) have gained recognition as highly suitable candidates for practical optoelectronics, primarily due to their narrower bandgap and broader spectrum absorption.[6] However, a significant challenge arises as the surface-to-volume ratio increases with shrinking size, resulting in intensified surface defects that eventually dominate the environmental phase stability of $CsPbI_3$ NWs.[7] Essentially, the black phase (α, β, and γ) of $CsPbI_3$ NWs tends to undergo a strong transformation to the yellow phase (δ, non-perovskite structure) at room temperature (RT).[8] In previous research, diverse strategies, such as surface modification and the introduction of other metal dopants, have been utilized to achieve the stabilization of the black phase in $CsPbI_3$ NWs.[9] In general, introducing Zn dopants has been documented as an efficient means to curb vacancy formation within halide perovskites,[11] reducing surface defects and impeding degradation triggered by external factors. The intriguing query arises as to whether this specific cation doping approach can equally impede the detrimental phase conversion of $CsPbI_3$, ensuring the operational phase stability of $CsPbI_3$ NWs.

In this study, we utilized density functional theory (DFT) calculations to anticipate that the Zn dopants not only suppress the vacancy formation but also stabilize the black phase structure for $CsPbI_3$ NWs. Through the VLS routes, we successfully designed and realized the out-of-plane growth of Zn-doped and self-catalyzed $CsPbI_3$ NWs. The beneficial effect of Zn doping on the $CsPbI_3$ NWs was confirmed via a series of surface characterization technologies. Moreover, photodetector devices utilizing these two types of NWs were also manufactured, showcasing the beneficial impact of Zn doping on the optoelectronic characteristics of pure $CsPbI_3$. Importantly, we revealed the polarization-sensitive characteristics of stable $CsPbI_3$ NWs, illustrating the

D. Li, P. Xie, Y. Zhang, Y. Meng, Y. Chen, Y. Zheng, W. Wang, D. Yin, B. Li, Z. Wu, D. Lei, F.-R. Chen, J. C. Ho
Department of Materials Science and Engineering
City University of Hong Kong
Kowloon 999 077, Hong Kong

C. Lan
State Key Laboratory of Electronic Thin Films and Integrated Devices
University of Electronic Science and Technology of China
Chengdu 610 054, China

S. Yip, J. C. Ho
Institute for Materials Chemistry and Engineering
Kyushu University
Fukuoka 816 8580, Japan
E-mail: johnnyho@cityu.edu.hk

J. C. Ho
Department of Materials Science and Engineering, and State Key Laboratory of Terahertz and Millimeter Waves
City University of Hong Kong
Kowloon 999077, Hong Kong

DOI: 10.1002/adfm.202314309

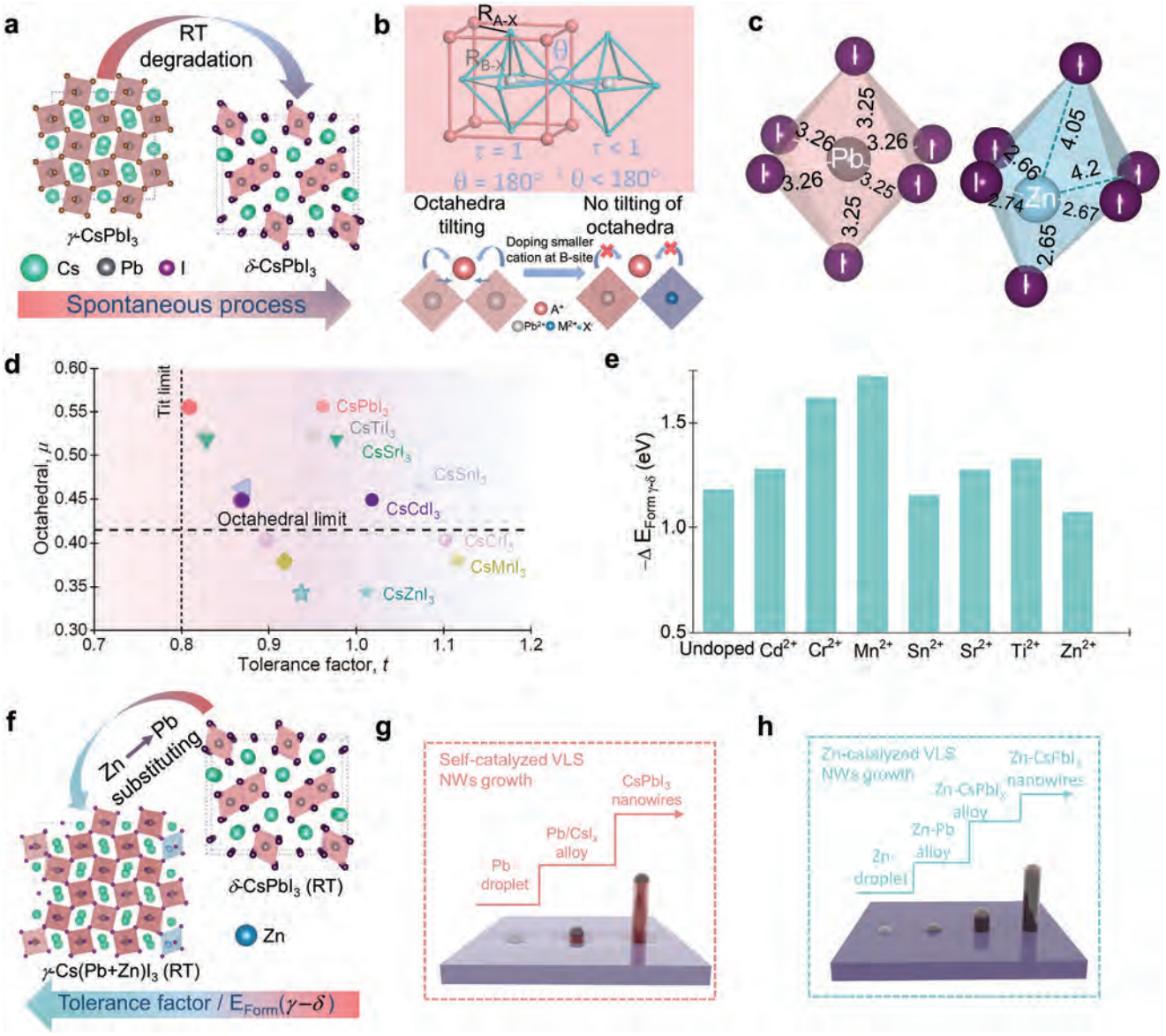

Figure 1. a) Schematic diagram of the spontaneous room temperature degradation of $CsPbI_3$. b) Schematic diagram of the relationship between the tolerance factor (τ) and the B—X—B bond angle. The bottom image shows how tilting of $[PbX_6]^{4-}$ octahedra is restricted with partial Pb^{2+} being substituted by smaller B-site cations. c) Metal—iodide bond distances for $CsPbI_3$ and partial $CsZnI_3$ in the optimized $CsPbI_3$ structure. d) The distribution of perovskites (ABX_3) containing metal centers including Pb, Ti, Sr, Sn, Cd, Cr, Mn, and Zn in relation to the Goldschmidt octahedral constraints and the tolerance factor. The left part is calculated through ionic radius, while the other part is calculated through bond distances. e) Histograms comparing the formation energy of phase transition ($\Delta E_{form\ \gamma\text{-}\delta}$) in initial $CsPbI_3$ and its doped structure with substituent 4.17% of various B-site cations. f) Schematic diagram of the improved thermal stability of orthorhombic $CsPbI_3$ by substituting partial Pb^{2+} with Zn^{2+}. g,h) Schematic diagram of the self-catalyzed and Zn-catalyzed VLS NWs growth.

optoelectronic anisotropic nature of $CsPbI_3$ NWs. Our work highlights the importance of impurity doping engineering for $CsPbI_3$ NWs and their further applications in anisotropic electronics.

According to previous research,[8] the metastable γ phase of $CsPbI_3$ will degrade spontaneously to the stable δ phase at RT (**Figure 1a**). Viewing from the environment, the degradation process of halide perovskite materials generally commences due to defects stemming from halide vacancies. These structural imperfections display a pronounced affinity for water and oxygen molecules; even a minimal concentration of such defects yields significant adverse effects.[10] Notably, leveraging its compact ionic radius and low electronegativity, incorporating Zn dopants has demonstrated a compelling capacity to mitigate vacancy formation.[11] This leads to a reduction in defect sites, consequently enhancing the stability of Zn-doped perovskite structures.

In essence, one significant structural aspect that influence the stability is the Goldschmidt's rule, $\tau = \frac{R_{A-X}}{\sqrt{2}R_{B-X}}$. Herein, R_{A-X}

denotes the separation between the A-site cation and the X-site anion, whereas R_{B-X} signifies the spacing between the B-site cation and the X-site anion (Figure 1b). The dimensions of the $[BX_6]^{4-}$ octahedra and the cubo-octahedral voids with regard to the A-site cation are influenced by the B-site cation. Under ideal conditions, a 180° bond angle between B–X–B is achieved, resulting in a cubic perovskite phase with a tolerance factor (τ) of 1.[12] However, for $CsPbI_3$, the Cs^{2+} ion is much smaller than the cubo-octahedral void size, resulting in a τ value of <1. As a result, the $[PbI_6]^{4-}$ octahedra undergoes rotation and tilt to minimize the excess space around the Cs^{2+} ion, causing the bond angle (θ) to be <180°.[13] But with partial Pb^{2+} being substituted by smaller B-site cations, the dimensions of the $[BX_6]^{4-}$ octahedra can be reduced, thus decreasing the void's size and realizing the whole structure's relative stability.

To shed light on the octahedral rotation process, DFT calculation was carried out to predict the lattice structure of the initial γ phase $CsPbI_3$ and its doped phase with partial substituents, including Cd^{2+}, Cr^{2+}, Mn^{2+}, Sn^{2+}, Sr^{2+}, Ti^{2+}, and Zn^{2+} (Figure 1d; Figure S1, Supporting Information). Typically, the substituent $[ZnI_6]^{4-}$ octahedra exhibits remarkable distortion in the optimized model, greatly hindering the further tilting or rotation of octahedra to achieve the stabilization of the black phase (Figure 1b). The localized distortion within the $CsPbI_3$ lattice results in an asymmetrical differential charge density encompassing Zn (Figure S2, Supporting Information). The specific geometry for Pb and distorted Zn octahedra are provided in Figure 1c. Meanwhile, the ionic radii constraints for the B^{2+} and I^- sites to stabilize octahedral coordination were also considered for all doped structures. More importantly, the formation energy of phase transition ($\Delta E_{form\ \gamma\text{-}\delta}$, defined as the energy change from γ phase to δ phase) was calculated and displayed in Figure 1e, indicating the suppression effect of Zn substitution to the deteriorative phase transition compared to initial perovskites and other doped structures. Hence, all calculated results suggest a promising prospect of the Zn doping strategy to stabilize the $CsPbI_3$ NWs (Figure 1f).

Inspired by the above analysis and calculations, initial $CsPbI_3$ and Zn-doped NWs design follow a VLS route based on chemical vapor deposition (CVD). Figure 1g,h depict schematic diagrams of the VLS growth process. The detailed NW growth process can be found in the Methods section, and a schematic diagram of the growth system is provided in Figure S3 (Supporting Information). Notably, the self-catalyzed VLS growth involves the formation of Pb seeds driven by surface energy induced by surface roughness, while the Zn nanocatalysts are synthesized through a drop-coating process. The dark field optical image of the substrate full of Zn nanoparticles is provided in Figure S4 (Supporting Information).

To verify the growth morphology and mechanism of the obtained NWs, the samples synthesized from these two routes were observed through a scanning electron microscope (SEM). As shown in Figure S5 (Supporting Information), the designed perovskite NWs from both routes were grown vertically (i.e., out of plane) on the substrate. Furthermore, as depicted in Figure S6 (Supporting Information), distinctive flower-like and spherical catalytic seeds can be observed in the tip region of each individual NW from the Zn-doped and self-catalyzed routes, respectively. Furthermore, the elemental distribution of the fabricated nanowire samples was examined through energy-dispersive X-ray spectroscopy (EDS) mapping (**Figure 2**a,b), revealing that the flower-like catalyst apex of the Zn-doped NW is primarily consisting of Zn. In contrast, the spherical catalytic seed of the self-catalyzed NW consists predominantly of Pb. Meanwhile, Cs, Pb, and I exhibit uniform distribution in the NW body for both samples. This result is expected as the melting temperatures of both the Zn-Pb alloying (183–245 °C) and pure lead (327.5 °C) are relatively low,[14] enabling the formation of liquid metal seeds together with a highly effective supersaturation mechanism occurring at the catalyst apex. On the other hand, the result reveals the limited solubility of the Cs and I at equilibrium in the liquid Zn and Pb during the growth of NWs. Hence, the NWs from these two routes have been verified as VLS growth. Composition quantification of the Zn-doped NWs was carried out along the axial axis of the NW (Figure 2c), confirming the uniform dispersion of Cs, Pb, and I elements within the NW body with a compositional ratio of 1:1:3, aligning with the stoichiometric ratio of $CsPbI_3$.

Next, to verify the crystal phase of these two obtained perovskite NWs, X-ray diffraction (XRD) was first carried out. As shown in Figure 2d, the main peaks of both NWs agree with the orthorhombic $CsPbI_3$ (Pnma (62), a = 8.856 Å, b = 8.576 Å, c = 12.472 Å).[15] The theta shift of peaks caused by Zn dopants was also noticed, indicating a smaller crystalline structure than the pristine $CsPbI_3$. Moreover, as depicted in scanning transmission electron microscopy (STEM) images (Figure S5, Supporting Information), the Zn-catalyzed $CsPbI_3$ NWs demonstrate significantly improved morphology compared to the self-catalyzed NWs, which exhibit irregular distortion and partial breakage in certain sections of their structure. The experimental results directly demonstrate the optimized effect of Zn-doping engineering on the environmental stability of $CsPbI_3$ NWs. Meanwhile, the acquired high-resolution TEM (HRTEM) image in Figure S7a (Supporting Information) confirms the orthorhombic phase of $CsPbI_3$ (Pnma (62)), which is further supported by the selected area electron diffraction (SAED) pattern shown in Figure S7b (Supporting Information), where the NW body's pattern corresponds to the (001) plane of the orthorhombic phase. These findings align well with the XRD results depicted in Figure 2d. Importantly, the orthorhombic perovskite structure of Zn-catalyzed $CsPbI_3$ NWs remains stable at room temperature, mainly due to the combined effect of substituted Zn^{2+} to Pb^{2+} and the larger I^- ionic radius compared to other halide ions.[16] Besides, the SAED pattern also reveals that the Zn-seeded $CsPbI_3$ NWs tend to grow along the [100] direction, aligning with prior experimental and computational investigations. This preference for growth along the (100) planes of $CsPbI_3$ NWs can be due to their reduced surface free energy compared to other crystallographic planes, which drives directed crystal growth.[17] In summary, the analysis of the structure and elements confirms that the acquired NW samples were $CsPbI_3$ orthorhombic phase grown following the VLS mechanism.

To investigate the impact of Zn impurity doping on the inherent properties of perovskites, we conducted photoluminescence (PL) measurements and analysis on samples of self-catalyzed and Zn-seeded $CsPbI_3$ NWs. As depicted in Figure 2e, the self-catalyzed $CsPbI_3$ NW exhibited a complete emission with full width at half-maximum (FWHM) of 31 nm, centered at 702 nm (≈1.766 eV), while the emission peak of Zn-seeded samples

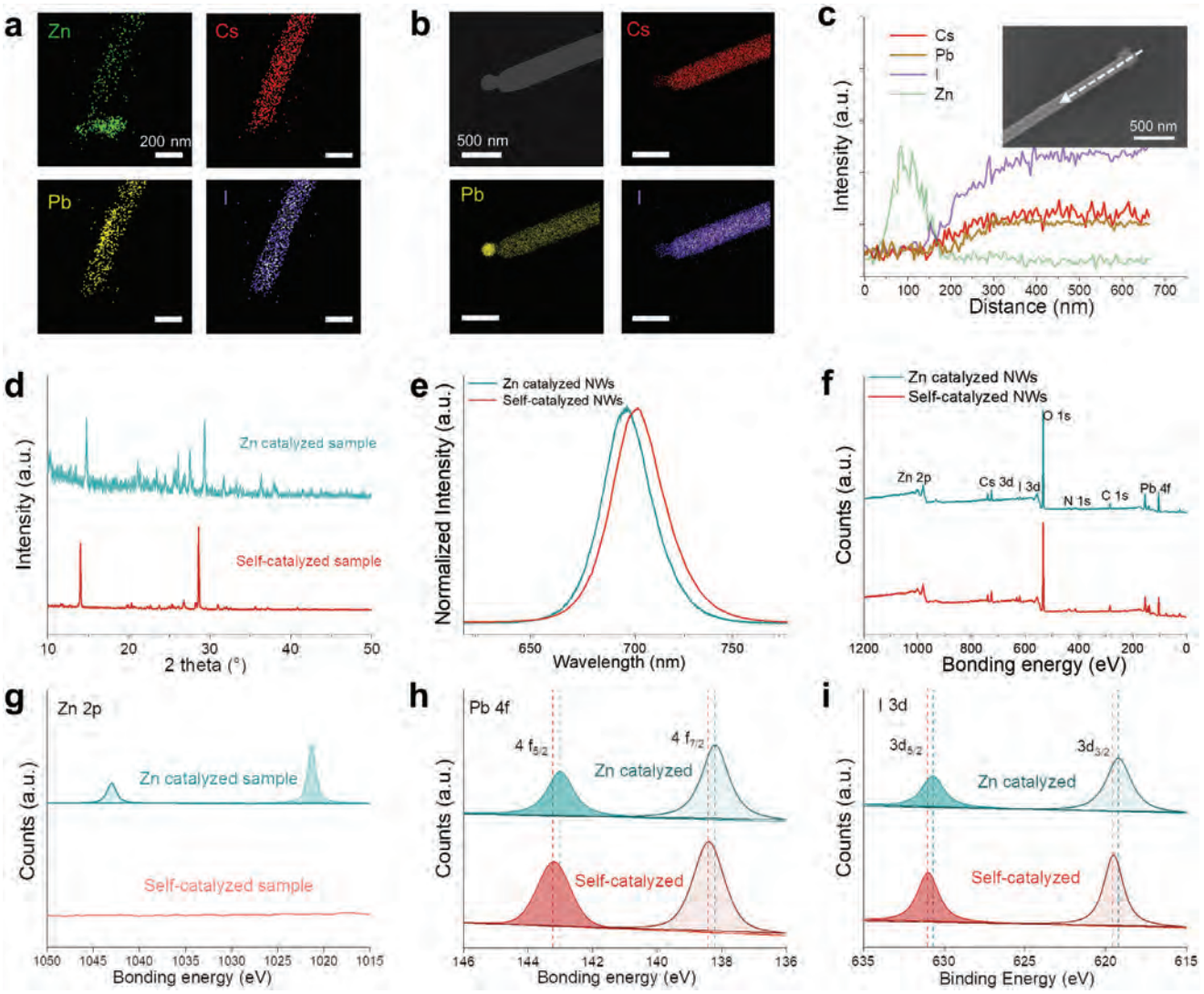

Figure 2. Materials characterization of the two types of $CsPbI_3$ NWs. a,b) EDS mapping of the Zn-catalyzed and self-catalyzed $CsPbI_3$ NWs. c) EDS line scan of the Zn-doped $CsPbI_3$ NWs. d) XRD spectra comparison of the Zn-catalyzed and self-catalyzed NWs. e) PL spectra of the two types of NWs. f–i) XPS spectra of the two types of $CsPbI_3$ NWs.

displayed a ≈6 nm blue shift. Previous theoretical studies have indicated that the $CsPbI_3$ lattice contracts due to the substitution of smaller Zn^{2+} cations for Pb^{2+}, also consistent with the observed theta shift in the XRD pattern of Zn-seeded NWs.[18] At the same time, the calculated bandgaps of Zn-doped perovskites (**Figure 3**e) have demonstrated a broadening, which can be attributed to a decrease in the volume of unit cell or/and an increase in electronegativity (EN) of the component species.[19] Meanwhile, the absorption and temperature-dependence PL of perovskite NW samples, both with and without Zn dopants, were measured to investigate the influence of Zn dopants. The results, as illustrated in Figure S8a,b (Supporting Information), further highlight the observed blue shift in the Zn-doped NWs, confirming the effect of Zn doping. The Zn-doped samples also exhibit superior thermal stability compared to the intrinsic perovskite samples. Notably, the intrinsic perovskite samples experience a PL intensity reduction of over 50% as the environmental temperature reaches 200 °C, whereas the Zn-doped samples demonstrate relative resilience under similar conditions.

To investigate the chemical states of Zn^{2+} within the NWs, these two NWs samples were investigated using X-ray photoelectron spectroscopy (XPS). Figure 2f displays XPS peaks for Cs, Pb, and I in both types of NWs. Notably, additional peaks were observed in the high-resolution XPS spectra of Zn 2p as shown in Figure 2g, appearing at 1021.2 and 1043 eV in the Zn-catalyzed $CsPbI_3$ NW sample, corresponding to the Zn 2p signals originating from Zn^{2+}. This observation indicates the incorporation of Zn^{2+} ions into the structure of $CsPbI_3$ NWs during the VLS growth process. To explore the impact of Zn on $CsPbI_3$ NWs further, we analyzed the high-resolution XPS spectra for Pb 4f and I 3d signals. In Figure 2h, the Pb 4f spectra of the self-catalyzed sample exhibited characteristic peaks corresponding to Pb^{2+} $4f_{7/2}$ and Pb^{2+} $4f_{5/2}$ at 138.3 and 143.2 eV, respectively. In contrast, those peaks of the Zn-catalyzed sample shifted to lower

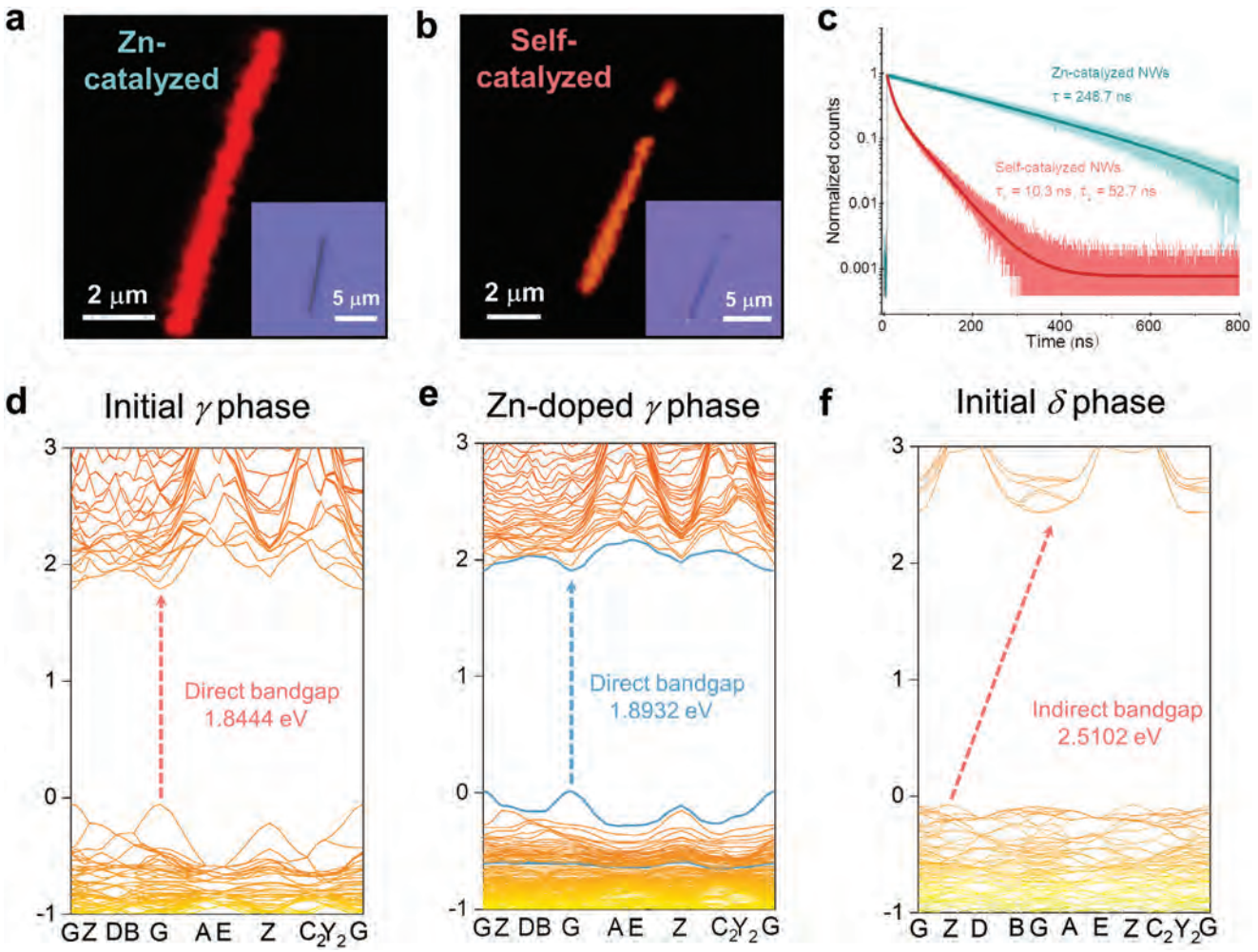

Figure 3. a,b) PL mapping (inset are the optical images) and c) TRPL curves of the two types of $CsPbI_3$ NWs. d–f) Calculated band of the initial γ, Zn-doped γ , and initial δ phase of the $CsPbI_3$.

energy levels. A similar shift was also observed in the I 3d spectra. The ≈0.2 eV decrease in the Pb^{2+} 4f and I 3d spectra of the Zn-catalyzed sample is attributed to the presence of Zn, demonstrating the incorporation of Zn^{2+} ions into the $CsPbI_3$ perovskite lattice. Furthermore, Zn^{2+} exhibits a more substantial chemical interaction with I^- compared to Pb^{2+}, potentially resulting in a partial weakening of the interaction between outer and core electrons in adjacent Pb^{2+} and I^- ions.[20]

To achieve a more in-depth exploration of the impact of Zn doping on $CsPbI_3$ NWs, we employed confocal photoluminescence (PL) mapping on both types of NWs (Figure 3a,b). The Zn-doped $CsPbI_3$ NWs exhibited complete and uniform PL signals across their entire bodies, while the self-catalyzed sample showed partial darkening and fragmenting PL mappings under the same measurement conditions. Time-resolved photoluminescence (TRPL) measurements were performed on the two types of $CsPbI_3$ NWs. Notably, they exhibited distinct TRPL decay characteristics. The Zn-seeded NW demonstrates a single-exponential fitting curve (τ = 248.7 ns), while the self-catalyzed NW exhibits a double-exponential TRPL decay characteristic ($\tau_{average} = \Sigma_i A_i {\tau_i}^2 / \Sigma_i A_i \tau_i$ = 36.5 ns). The simpler PL decay and increased PL lifetime observed in the Zn-catalyzed NW indicate the suppression of nonradiative recombination, indicating a lower defect density surface compared to the self-catalyzed NW.[21] The presence of trapping states induced by defects in the nonradiative recombination process captures photogenerated carriers and reduces their diffusion length, leading to inferior optoelectronic performance.[22] Therefore, the superior surface condition of Zn-catalyzed $CsPbI_3$ NWs holds the potential for good performance and high-speed optoelectronics.

Following that, the optoelectronic properties of the two types of $CsPbI_3$ NWs were investigated by configuring them into photodetector (PD) devices (detailed procedures compiled in Figure S9 and Method section, Supporting Information).[5,23] The specific schematic diagram and SEM image are provided in **Figure** 4a,b. In the current-voltage (*I-V*) curves (Figure 4c) and current versus time (*I-t*) curves (Figure 4d), the Zn-seeded $CsPbI_3$ NW PDs exhibit ultra-low dark currents (I_{dark}) of ≈0.1 pA at 2 V bias. At the same time, the self-catalyzed NW devices have dark currents (I_{dark}) that increased over 10 times. However, under a 2 mW cm^{-2} illumination of 450 nm laser, the photocurrent (I_{light}) of Zn-catalyzed $CsPbI_3$ NW devices increases by over 10^4 times to

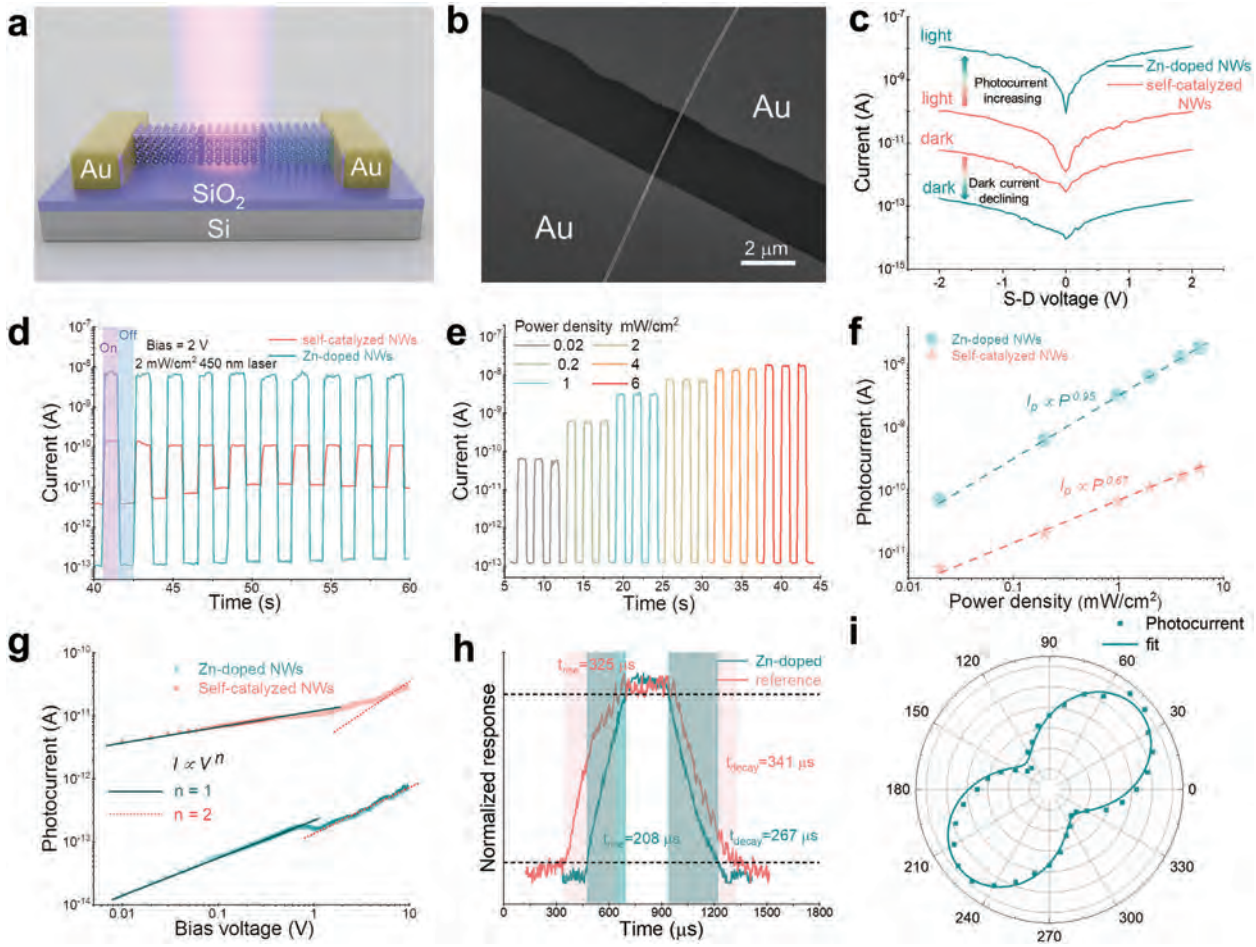

Figure 4. Device performance characterization. a,b) Schematic diagram and SEM image of the single NW PD device. c) *I-V* curve and d) I-t curve comparison of the two types of NW PD devices. e) *I-t* curve of the Zn-doped PD device under different power density illumination. f) *I-P* curve, g) SCLC curve, h) response and recovery times curve comparison of the two types of NW PD devices. i) Polarization dependence of the current intensity at the bias of 2 V and light intensity of 2 mW cm^{-2}.

5.7 ± 0.4 nA, much higher than the self-catalyzed PD devices, at ≈10 times. Moreover, the photoresponse (Figure 4e) was investigated at various power densities (spanning from 0.02 to 6 mW cm^{-2}), demonstrating a positive correlation between photocurrent and power density as more carriers are generated with an increasing photon flux. All the photocurrent data for the two types of PDs were extracted and compiled in Figure 4f, fitting perfectly to the power law equation of $I_{ph} \propto P^{\alpha}$. The coefficient α values of Zn-doped and self-catalyzed NW PDs are calculated to be 0.67 and 0.95, respectively, indicating an ideal trap-free characteristic of Zn-doped NWs.[24]

To evaluate the optoelectronic performance of the two types of NW-based PDs, the two most important figure-of-merit parameters, responsivity (R) and detectivity (D^*), were calculated. Here, R is described by the equation $R = I_{ph}/PS$, where I_{ph} ($I_{ph} = I_{light} - I_{dark}$), P, and S are the photocurrent, power density, and effective illumination area, respectively. Under the illumination of 0.02 mW cm^{-2}, the highest R-value for Zn-seeded $CsPbI_3$ NWs is 1935 ± 55 A W^{-1}(Figure S10a, Supporting Information), which is larger than the self-catalyzed $CsPbI_3$ NW value of 98 ± 18 A W^{-1} under the same conditions. The other parameter, D^*, is described as $D^* = R(S\,\Delta f)^{1/2}/i_n$. Here, Δf represents the electrical bandwidth, and i_n represents the noise current. According to Figure S10c (Supporting Information), the noise current spectrum is primarily characterized by 1/f noise when biased at 2 V. Moreover, there is a noticeable noise enhancement from 1.53 fA $Hz^{-1/2}$ of Zn-catalyzed PDs to 98.44 fA $Hz^{-1/2}$ of the self-catalyzed device at 1 Hz, which can be attributed to the stabilization of Zn impurity dopants to suppress the phase transition degradation process. The highest D^* (Figure S10b, Supporting Information) of Zn-catalyzed PDs is calculated as 5.97×10^{13} cm $Hz^{1/2}W^{-1}$ (Jones), higher than the self-catalyzed device of 4.58×10^{10} Jones and outperforming most reported 1D perovskite devices (Figure S10d and Table S1, Supporting Information). Furthermore, a fast response is also important for a practical PD. In essence, the response time is mainly dominated by photogenerated carriers' separation, transport, and collection efficiency.[25] To acquire the high-precision photoresponse, a current amplifier and digital oscilloscope were connected to the device to record the high-speed signals achieved by a 800 Hz chopper.[26] As depicted in Figure 4f, the Zn-catalyzed $CsPbI_3$ NW exhibits an impressively fast photoresponse of 208 μs, surpassing the self-catalyzed

$CsPbI_3$ NW with 325 µs, as well as most of the reported 1D perovskite (Table S1 and Figure S10e, Supporting Information). The significantly higher performance of Zn-catalyzed NWs can be attributed to superior material quality, meanwhile preventing the degradation transmission from the black phase to the yellow phase.

Moreover, a detailed analysis of the space-charge-limited current (SCLC) results (Figure 4h) was conducted to evaluate the surface condition of NWs further. Drawing on the previous research work,[27] the trap-filled limit voltage (V_{TFL}) is primarily influenced by the trap density (n_t) as,

$$V_{TFL} = \frac{en_tL^2}{2\varepsilon\varepsilon_0} \quad (1)$$

where L, ε (assumed as 6.3)[28] and ε_0 are the channel length, the relative dielectric constant of $CsPbI_3$, and the vacuum permittivity, respectively. The trap density, n_t, of Zn-doped $CsPbI_3$ was computed as 4.04×10^{14} cm^{-3}, which is lower than that of self-catalyzed samples (1.73×10^{15} cm^{-3}), signifying an improved electron transport pathway in Zn-catalyzed $CsPbI_3$. Therefore, it was demonstrated that the effectiveness of the Zn doping strategy in stabilizing the $CsPbI_3$ NWs and reducing the trap density, ultimately optimizing the corresponding optoelectronic performance.

Moreover, the polarized photoelectric behavior of the Zn-doped device was investigated further to reveal the underlying optical anisotropy of Zn-doped $CsPbI_3$ NWs. The polarization-dependent photoresponse measurements were performed by positioning a 1/2 polarizer before the 450 nm laser as the polarization photosource. Figure 4i and Figure S10f (Supporting Information) illustrate the corresponding polarization photoresponse at a bias of 2 V and light intensity of 2 mW cm^{-2}, demonstrating varying photocurrent intensities with the laser polarization angle from 0° to 360°. The photocurrent enhances to a maximum at 45° and 225° polarization angles and reduces to the minimum values at 135° and 315°. Therefore, the photoresponse anisotropy ratio, ε, of the Zn-doped $CsPbI_3$ can be calculated through $\varepsilon = (I_{max} - I_{min})/(I_{max} + I_{min})$ as 0.68,[29] indicating the great potential of the Zn-doped $CsPbI_3$ NWs for the polarization-sensitive optoelectronic devices.

In this work, the VLS growth of single-crystal $CsPbI_3$ NWs was achieved through self-catalyzed and Zn-catalyzed routes. DFT calculations and a series of characterization technologies revealed the optimization effect of Zn impurity doping on the degradation of $CsPbI_3$NWs. The single $CsPbI_3$ NW was configured into PDs, exhibiting remarkable optoelectronic performances, achieving a remarkable responsivity of 1935 A W^{-1}, ≈10^5 on/off current ratio, a detectivity of 5.97×10^{13} Jones, and a fast response time of 206 µs. Importantly, the Zn-catalyzed perovskite nanowires exhibit apparent photoresponse anisotropy, promising for fundamental investigations and practical applications.

Supporting Information

Supporting Information is available from the Wiley Online Library or from the author.

Acknowledgements

D.L. and P.S.X. contributed equally to this research, which was financially supported by a fellowship grant (CityU RFS2021-1S04) and a Collaborative Research Equipment Grant (C1015-21EF), both awarded by the Research Grants Council of the Hong Kong Special Administrative Region, China.

Conflict of Interest

The authors declare no conflict of interest.

Data Availability Statement

The data that support the findings of this study are available from the corresponding author upon reasonable request.

Keywords

halide perovskite, nanowire, optoelectronic anisotropy, vacancy suppressor, Zn-doping

Received: November 14, 2023
Revised: December 26, 2023
Published online:

[1] a) L. Gu, S. Poddar, Y. Lin, Z. Long, D. Zhang, Q. Zhang, L. Shu, X. Qiu, M. Kam, A. Javey, *Nature* **2020**, *581*, 278; b) D. Zhang, Q. Zhang, B. Ren, Y. Zhu, M. Abdellah, Y. Fu, B. Cao, C. Wang, L. Gu, Y. Ding, *Nat. Photonics* **2022**, *16*, 284; c) Y. Zhang, S. Poddar, H. Huang, L. Gu, Q. Zhang, Y. Zhou, S. Yan, S. Zhang, Z. Song, B. Huang, *Sci. Adv.* **2021**, *7*, eabg3788.
[2] M. Shoaib, X. Zhang, X. Wang, H. Zhou, T. Xu, X. Wang, X. Hu, H. Liu, X. Fan, W. Zheng, *J. Am. Chem. Soc.* **2017**, *139*, 15592.
[3] Q. Zhang, D. Zhang, L. Gu, K.-H. Tsui, S. Poddar, Y. Fu, L. Shu, Z. Fan, *ACS Nano* **2020**, *14*, 1577.
[4] J. Chen, Y. Fu, L. Samad, L. Dang, Y. Zhao, S. Shen, L. Guo, S. Jin, *Nano Lett.* **2017**, *17*, 460.
[5] Y. Meng, C. Lan, F. Li, S. Yip, R. Wei, X. Kang, X. Bu, R. Dong, H. Zhang, J. C. Ho, *ACS Nano* **2019**, *13*, 6060.
[6] a) C.-K. Lin, Y. Zhang, M. Gao, J.-A. Lin, H. K. Le, Z. Lin, P. Yang, *Nano Lett.* **2022**, *22*, 2437; b) Z. Long, X. Qiu, C. L. J. Chan, Z. Sun, Z. Yuan, S. Poddar, Y. Zhang, Y. Ding, L. Gu, Y. Zhou, *Nat. Commun.* **2023**, *14*, 1972.
[7] a) M. Lai, Q. Kong, C. G. Bischak, Y. Yu, L. Dou, S. W. Eaton, N. S. Ginsberg, P. Yang, *Nano Res.* **2017**, *10*, 1107; b) J. Xue, R. Wang, Y. Yang, *Nat. Rev. Mater.* **2020**, *5*, 809.
[8] J. A. Steele, H. Jin, I. Dovgaliuk, R. F. Berger, T. Braeckevelt, H. Yuan, C. Martin, E. Solano, K. Lejaeghere, S. M. Rogge, *Science* **2019**, *365*, 679.
[9] a) J. A. Steele, V. Prakasam, H. Huang, E. Solano, D. Chernyshov, J. Hofkens, M. B. Roeffaers, *J. Am. Chem. Soc.* **2021**, *143*, 10500; b) Y. Fu, M. T. Rea, J. Chen, D. J. Morrow, M. P. Hautzinger, Y. Zhao, D. Pan, L. H. Manger, J. C. Wright, R. H. Goldsmith, *Chem. Mater.* **2017**, *29*, 8385; c) S. Masi, A. F. Gualdrón-Reyes, I. Mora-Sero, *ACS Energy Lett.* **2020**, *5*, 1974.
[10] J. Jeong, M. Kim, J. Seo, H. Lu, P. Ahlawat, A. Mishra, Y. Yang, M. A. Hope, F. T. Eickemeyer, M. Kim, *Nature* **2021**, *592*, 381.
[11] M. I. Saidaminov, J. Kim, A. Jain, R. Quintero-Bermudez, H. Tan, G. Long, F. Tan, A. Johnston, Y. Zhao, O. Voznyy, *Nat. Energy* **2018**, *3*, 648.

[12] A. Swarnkar, W. J. Mir, A. Nag, *ACS Energy Lett.* **2018**, *3*, 286.
[13] M. C. Brennan, J. E. Herr, T. S. Nguyen-Beck, J. Zinna, S. Draguta, S. Rouvimov, J. Parkhill, M. Kuno, *J. Am. Chem. Soc.* **2017**, *139*, 12201.
[14] R. Goswami, K. Chattopadhyay, *Philos. Mag. Lett.* **1993**, *68*, 215.
[15] R. J. Sutton, M. R. Filip, A. A. Haghighirad, N. Sakai, B. Wenger, F. Giustino, H. J. Snaith, *ACS Energy Lett.* **2018**, *3*, 1787.
[16] Y. Meng, Y. Zhang, Z. Lai, W. Wang, W. Wang, Y. Li, D. Li, P. Xie, D. Yin, D. Chen, *Nano Lett.* **2022**, *23*, 812.
[17] G. Niu, H. Yu, J. Li, D. Wang, L. Wang, *Nano Energy* **2016**, *27*, 87.
[18] W. Van der Stam, J. J. Geuchies, T. Altantzis, K. H. Van Den Bos, J. D. Meeldijk, S. Van Aert, S. Bals, D. Vanmaekelbergh, C. de Mello Donega, *J. Am. Chem. Soc.* **2017**, *139*, 4087.
[19] I. E. Castelli, J. M. García-Lastra, K. S. Thygesen, K. W. Jacobsen, *APL Mater.* **2014**, *2*, 081514.
[20] X. Shen, Y. Zhang, S. V. Kershaw, T. Li, C. Wang, X. Zhang, W. Wang, D. Li, Y. Wang, M. Lu, *Nano Lett.* **2019**, *19*, 1552.
[21] a) L. Shen, Y. Fang, D. Wang, Y. Bai, Y. Deng, M. Wang, Y. Lu, J. Huang, *Adv. Mater.* **2016**, *28*, 10794; b) J. I. Khan, F. H. Isikgor, E. Ugur, W. Raja, G. T. Harrison, E. Yengel, T. D. Anthopoulos, S. De Wolf, F. Laquai, *ACS Energy Lett.* **2021**, *6*, 4155.
[22] a) X. Zheng, B. Chen, J. Dai, Y. Fang, Y. Bai, Y. Lin, H. Wei, X. C. Zeng, J. Huang, *Nat. Energy* **2017**, *2*, 1; b) X. Zhu, M. Du, J. Feng, H. Wang, Z. Xu, L. Wang, S. Zuo, C. Wang, Z. Wang, C. Zhang, *Angew. Chem., Int. Ed.* **2021**, *60*, 4238.
[23] X. C. Li, Y. Meng, R. Fan, S. F. Fan, C. Q. Dang, X. B. Feng, J. C. Ho, Y. Lu, *Nano Res.* **2021**, *14*, 4033.
[24] Y. Lee, D. Yoon, S. Yu, H. Sim, Y. Park, Y. S. Nam, K. J. Kim, S. Y. Choi, Y. Kang, J. Son, *Adv. Mater.* **2022**, *34*, 2107650.
[25] a) F. X. Liang, J. J. Jiang, Y. Z. Zhao, Z. X. Zhang, D. Wu, L. H. Zeng, Y. H. Tsang, L. B. Luo, *Adv. Funct. Mater.* **2020**, *30*, 2001033; b) L. H. Zeng, Q. M. Chen, Z. X. Zhang, D. Wu, H. Yuan, Y. Y. Li, W. Qarony, S. P. Lau, L. B. Luo, Y. H. Tsang, *Adv. Sci.* **2019**, *6*, 1901134.
[26] a) Y. Meng, Z. Lai, F. Li, W. Wang, S. Yip, Q. Quan, X. Bu, F. Wang, Y. Bao, T. Hosomi, *ACS Nano* **2020**, *14*, 12749; b) D. Li, C. Lan, A. Manikandan, S. Yip, Z. Zhou, X. Liang, L. Shu, Y.-L. Chueh, N. Han, J. C. Ho, *Nat. Commun.* **2019**, *10*, 1664.
[27] Q. Dong, Y. Fang, Y. Shao, P. Mulligan, J. Qiu, L. Cao, J. Huang, *Science* **2015**, *347*, 967.
[28] L. Protesescu, S. Yakunin, M. I. Bodnarchuk, F. Krieg, R. Caputo, C. H. Hendon, R. X. Yang, A. Walsh, M. V. Kovalenko, *Nano Lett.* **2015**, *15*, 3692.
[29] Y. Wang, F. Yang, X. Li, F. Ru, P. Liu, L. Wang, W. Ji, J. Xia, X. Meng, *Adv. Funct. Mater.* **2019**, *29*, 1904913.